Incorporating mask topography edge diffraction in photolithography simulations

Jaione Tirapu-Azpiroz and Eli Yablonovitch

Department of Electrical Engineering, University of California, Los Angeles, California 90095

Received April 19, 2005; revised July 16, 2005; accepted August 24, 2005; posted September 26, 2005 (Doc. ID 61459)

In deep ultraviolet lithography simulations, conventional application of Kirchhoff's boundary conditions on the mask surface provides the so-called "thin-mask" approximation of the object field. Current subwavelength lithographic operation, however, places a serious limitation on this approximation, which fails to account for the topographical, or "thick-mask," effects. In this paper, a new simulation model is proposed that is theoretically founded on the well-established physical theory of diffraction. This model relies on the key result that diffraction effects can be interpreted as an intrinsic edge property, and modeled with just two fixed parameters: width and transmission coefficient of a locally determined boundary layer applied to each chrome edge. The proposed model accurately accounts for thick-mask effects of the fields on the mask, greatly improving the accuracy of aerial image simulations in photolithography, while maintaining a reasonable computational cost.

OCIS codes: 110.3960, 260.1960, 260.2110.

1. INTRODUCTION

In the evaluation of the fields diffracted by the reticle during optical lithography simulations, it has been customary to apply the so-called Kirchhoff's boundary conditions[1] to approximate the boundary value of the fields on the mask surface. These boundary conditions replace the fields on the patterned mask apertures by those that would exist in the absence of the screen. Direct application of Kirchhoff's boundary conditions provides a thin-mask approximation of the object field on the exit surface of the mask, obtained after multiplying the incident field by an ideal transmission function of the mask pattern.

The utilization of 193 nm-wavelength lithography with a 0.85 NA optical system to print 65 nm wafer features translates into k_1 factors[2] approaching values of ≈ 0.3 and mask features of the order of the wavelength for $4\times$ magnification. In addition, alternating-phase-shifting masks[3] employ etching profiles with abrupt discontinuities and trench depths also of the order of the wavelength. Rigorous three-dimensional (3D) electromagnetic simulations of the fields on the mask surface are extremely resource- and time-consuming, hence impractical even for small portions of the mask. The thin-mask model, on the other hand, ignores diffraction and polarization effects that, because of the wavelength-size mask topography, are becoming an increasing source of simulation errors in lithography.[4,5]

An alternative modeling approach is introduced in this paper that retains much of the thin-mask efficiency but accurately accounts for peak transmission and phase deviations of the electromagnetic field through the reticle apertures. Our model derives from the physical theory of diffraction (PTD), initially developed by Ufimtsev.[6] In PTD the total field scattered by a metallic object is evaluated by adding a "fringe" field generated by electric and magnetic equivalent edge currents along the edges of the scatterer to the physical optics (PO) or, equivalently through Babinet's principle,[1] to Kirchhoff's approximation on an aperture. We observed how the relative contribution of these fringe fields to the real and imaginary components of the electric field on the wafer are reciprocal to the mean size and height, respectively, of the openings which allowed us to reduce the model to a simple boundary strip of fixed width and transmission coefficient, added to the conventional Kirchhoff or thin-mask approximation. To account for the finite thickness and index of refraction of the chrome layer as well as for the reticle profile, the parameters of this boundary strip vary with the chrome specifications and the aperture cross section.

Several other methodologies have been explored in the literature that account for edge diffraction in lithographic simulations. Adam and Neureuther[7] proposed the domain decomposition method, in which the fields diffracted by isolated edges are precalculated and added afterwards according to the diffraction patterns. This method produces accurate results but with a heavy computational burden. Khoh *et al.*[8] proposed an approach based on the geometrical theory of diffraction (GTD) that separates the field diffracted by an aperture into a geometrical component and a boundary component in the form of rays emanating from the edge. The GTD formulation used in the approach of Khoh *et al.* is an asymptotic approximation, for high frequencies, of the PTD. It accurately incorporates edge diffraction but applies only to perfect electric conductors. The chrome layer that forms the reticle, however, has a finite index of refraction at the lithographic wavelength, which has a nonnegligible impact on the topography effects.[9]

This paper is organized as follows. Section 2 establishes the foundations of the model, which is further developed for its application in lithography in Section 3. Examples of enhanced modeling performance are presented in Section 4.

2. PHYSICAL THEORY OF DIFFRACTION APPLIED TO APERTURES ON CONDUCTING SCREENS

The interpretation of diffraction as the interference of the incident wave with a boundary wave generated at the object edge was suggested by Young prior to publication of the Huygens–Fresnel theory in 1818. Later, in 1896, Sommerfeld obtained a rigorous theoretical solution of the diffraction of an electromagnetic plane wave from a perfectly conducting half-plane. The asymptotic expansion of Sommerfeld's rigorous solution can be separated into a geometrical optics contribution in the form of the incident and reflected waves, and a boundary contribution in the form of a cylindrical wave emanating from the edge. This boundary diffraction wave propagates through both lit and shadow regions, hence rigorously confirming Young's ideas.

In a source-free homogeneous medium, a general solution of an electromagnetic scattering problem is obtained by adding to the incident fields the so-called scattered fields $\mathbf{E}^S$, $\mathbf{H}^S$ produced by equivalent induced sources on the scattering object's surface. The following common representation of the scattered electromagnetic field is known as the Franz formula[10]:

$$\mathbf{E}^S = -j\omega\mu\mathbf{A} - j\frac{1}{\omega\epsilon}\nabla(\nabla\cdot\mathbf{A}) - \nabla\times\mathbf{F}, \tag{1}$$

$$\mathbf{H}^S = -j\omega\epsilon\mathbf{F} - j\frac{1}{\omega\mu}\nabla(\nabla\cdot\mathbf{F}) + \nabla\times\mathbf{A}, \tag{2}$$

expressed here in terms of the vector potentials $\mathbf{A}$ and $\mathbf{F}$

$$\mathbf{A} = \int\int_S \mathbf{J}\frac{e^{ikr}}{4\pi r}ds, \tag{3}$$

$$\mathbf{F} = \int\int_S \mathbf{M}\frac{e^{ikr}}{4\pi r}ds, \tag{4}$$

generated by surface integration of the equivalent surface currents $\mathbf{J}=\hat{\mathbf{n}}\times\mathbf{H}$ and $\mathbf{M}=\mathbf{E}\times\hat{\mathbf{n}}$.

The PO approximation is similar to Kirchhoff's boundary conditions in that the field is assumed to be unperturbed by the boundaries of the scattering object. Kirchhoff's approach attempts to determine the field behind an opaque screen with an aperture and it can be shown to be equivalent, through Babinet's principle,[1,11] to the PO approximation on a conducting plate complementary to the aperture. In PTD, the PO approximation of the equivalent currents induced on the surface of a perfectly conducting scattering object $\mathbf{J}^{PO}$ is improved by adding a correction or fringe term $\mathbf{J}^{FR}$ due to the presence of the edge discontinuity. Based on Sommerfeld's rigorous solution for the field diffracted by a perfectly conducting edge, Ufimtsev[12] deduced the expression of this fringe current for metallic objects in terms of integrals in the complex plane. He observed that it concentrates mainly near the edge, but its decreasing tail extends to infinite distance over an infinitely narrow and infinitely long strip on the metal surface as indicated in Fig. 1(a). A similar formulation can be derived for the equivalent currents induced on an aperture in a conducting screen, that is, $\mathbf{M}=\mathbf{M}^K+\mathbf{M}^{FR}$, where the first term on the right-hand side represents the Kirchhoff approximation and the second term represents the fringe currents, both extending on the aperture surface as illustrated in Fig. 1(b). The fields generated by these fringe currents are obtained as

$$\mathbf{F}^{FR} = \int_C\int_0^\infty \mathbf{M}^{FR}\frac{e^{ikr}}{4\pi r}d\tau dl. \tag{5}$$

For perfect conductors and in the limit in which $kr\to\infty$, the surface integral (5) is reduced asymptotically to a line integral over the edge. Ufimtsev[12] provided expressions for the fringe fields, valid at every point in space.

We applied the asymptotic expression of Eq. (5), that is, Eq. (A1) (See Appendix A), to calculate the aperture fringe fields of a rectangular aperture of width w and height h on the perfectly conducting plate of Fig. 2. The resultant diffracted far field was then simulated to pass through an imaging system of 4× reduction factor such that, even with high NA, the angle formed by the diffraction orders collected at the entrance pupil can be assumed small.[13] Under these circumstances, it is observed that the correction term of the field attributed to the fringe fields obeys, at the center of the image plane ($x=y=0$), the relation

$$\mathbf{E}_{image} = \mathbf{E}^K_{image} + \mathbf{E}^{FR}_{image} = \mathbf{E}^K_{image}\left(1+\frac{\Delta\mathbf{E}}{\mathbf{E}}\right), \tag{6}$$

with

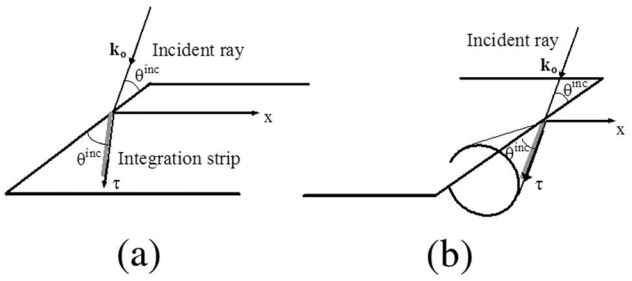

Fig. 1. (a) Geometry of a half-plane edge tangential to each point of the aperture edge. The integration strips on the metal surfaces along the diffraction cone are responsible for the edge waves diffracted by the object boundary. (b) Through Babinet's principle the integration strips are taken on the edge complementary aperture.

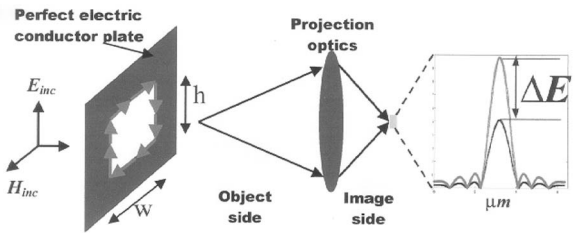

Fig. 2. Application of PTD to a rectangular aperture on perfectly electrically conducting plate and imaging through a 4×, NA=0.85 optical system. Relative error on the field amplitude due to edge diffraction is measured at the peak of the image.

$$\frac{\Delta \mathbf{E}}{\mathbf{E}} = \frac{\mathbf{E}^{\mathrm{FR}}_{\mathrm{image}}}{\mathbf{E}^{\mathrm{K}}_{\mathrm{image}}} \approx -\frac{j}{2k}\frac{(2h+2w)}{hw} = -\frac{j}{2k}\frac{4}{\frac{2hw}{w+h}} = -j\frac{4\Delta d}{d_{effective}}. \tag{7}$$

This result indicates that the relative error on the electric field amplitude due to the fringe fields, which are ignored in the Kirchhoff approximation, is inversely proportional to the effective opening size measured as the harmonic mean of the opening width w and height h. The harmonic mean is defined as twice the product of the sides divided by its sum. In other words, this inverse dependence of the relative error on the opening size can be expressed as the ratio of the area covered by a strip of width Δd placed along the edges of the openings to the total area of the opening, as outlined in

$$\frac{\Delta \mathbf{E}}{\mathbf{E}} = \frac{\mathbf{E}^{\mathrm{FR}}_{\mathrm{image}}}{\mathbf{E}^{\mathrm{K}}_{\mathrm{image}}} \approx -j\frac{(2h+2w)\Delta d}{hw} = -j\frac{\text{boundary layer area}}{\text{total area}}. \tag{8}$$

This last interpretation of Eq. (8) suggests a transformation of the infinite integral (5), expressed in terms of fringe currents, to a finite surface integral along the aperture boundary and on a layer of thickness Δd; that is

$$\mathbf{F}^{\mathrm{FR}} = -j\int_C \int_0^{\Delta d} \mathbf{M}^{\mathrm{K}} \frac{e^{ikr}}{4\pi r} \mathrm{d}\tau \mathrm{d}l, \tag{9}$$

where the equivalent current $\mathbf{M}^{\mathrm{FR}}$ is replaced by the simpler $\mathbf{M}^{\mathrm{K}}=\mathbf{E}^{inc}\times\hat{\mathbf{n}}$. When adding Eq. (9) to the Kirchhoff approximation, it can be graphically interpreted as a correction strip of width $\Delta d=1/2k$ and transmission coefficient $-j$ added to the edges of the aperture.

3. APERTURES ON THICK MASKS

The PTD, as well as the results of Section 2 that were derived from its application to apertures, considered infinitely thin, perfect conductors. The chrome layer where the photomask is patterned, however, has a finite index of refraction at the wavelengths of lithography operation and cannot be regarded as a perfect conductor. In addition, it has a finite thickness and is covered by a thick layer of glass that can be etched to create phase-shifting features on the mask as illustrated in Fig. 3. The trench of the 180°-shifter opening of Fig. 3 is etched to a depth such that light propagating through is exactly 180° out of phase relative to light propagating through the unetched or clear opening. As a consequence, the correction strip thickness $\Delta d=1/2k$ and transmission coefficient $-j$ in Eq. (8), deduced analytically for the ideal case of an infinitely thin perfect conductor, cannot be applied to approximate the field diffracted by photomasks.

In order to derive the parameters of a similar inverse relation of the Kirchhoff approximation error on the aperture effective size d, comparison of the aerial electric field at the focal plane produced by various phase-shifting thick masks with that produced by their corresponding ideal thin-mask models was performed for both clear and 180°-shifter openings. The relative error in amplitude resulting from the application of the Kirchhoff approximation to these structures was then measured at the peak of the aerial image field in a similar fashion to that in Section 2, and is illustrated in Fig. 4. Rigorous evaluation of the field on the surface of a 95-nm-thick chrome layer mask with an index of refraction at 193 nm wavelength equal to $0.84-j1.65$, and covered by a thick layer of 1.563 refractive-index glass, as illustrated in Fig. 3, was simulated through the finite-difference-time-domain software TEMPEST 6.0.[14] Next, a vectorial formulation of the imaging process was applied to evaluate the aerial images at the wafer plane generated by a 4× system with NA = 0.85 and operating at 193 nm.[13]

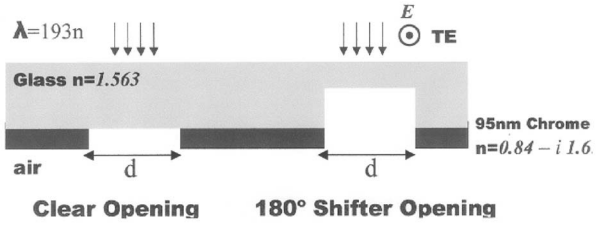

Fig. 3. Reticle cross sectional profile of typical alternating-phase-shifting masks.

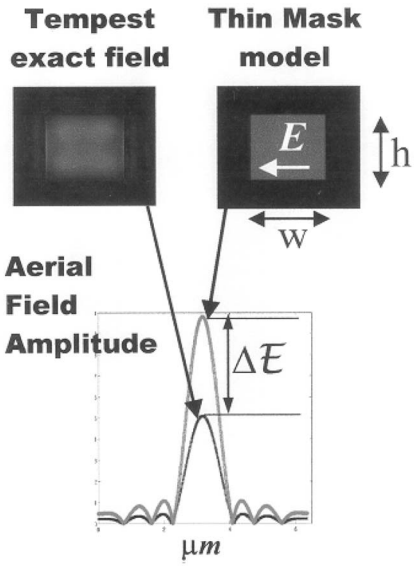

Fig. 4. Error measurement on aerial image field amplitude due to the thin-mask approximation relative to the rigorously evaluated mask field.

The error due to Kirchhoff approximation in the real and imaginary parts of the field's main polarization component was calculated separately. The deficit of the real component of the FDTD field relative to the thin-mask field for both square and rectangular openings illuminated by a coherent, normally incident, plane wave is shown in Fig. 5(a). It exhibits the same reciprocal dependence on the size of the opening (measured as the harmonic mean of its width w and height h) as was observed for apertures on perfectly conducting screens. This inverse relation can be formulated such that the error can be assumed proportional to an opaque correction width Δd derived, for each etching profile, from the slope of the best fitting straight line to the data points in Fig. 5(a), in

a least-squares sense. This relation is expressed in Eq. (10). Graphically, the real component of the Kirchhoff approximation should be modified with an opaque correction strip, uniform with the size of the opening and to be applied on all four sides of the thin mask model regardless of polarization, as illustrated in Fig. 6(a).

$$\text{Amplitude deficit} = \text{Re}\left\{\frac{\Delta \mathbf{E}}{\mathbf{E}}\right\} = -\frac{4\Delta d}{d} = -\frac{4\Delta d}{(2wh)/(w+h)}. \tag{10}$$

In a similar fashion, we found that an inverse law holds for the imaginary part of the error on the aerial image field due to the thin mask approximation versus the opening height h, defined as the side length in the direction perpendicular to the electric field polarization. This reciprocal relation is illustrated in Fig. 5(b). Some of the data points resulting from rectangular apertures with high aspect ratios still show some deviation from the fitting line; however, use of the harmonic mean or any other dimension rather than the opening height produced a poorer fit to the inverse law. It will be shown in Section 4 that significant error improvements are achieved for all cases, including those points with some deviation from the inverse law.

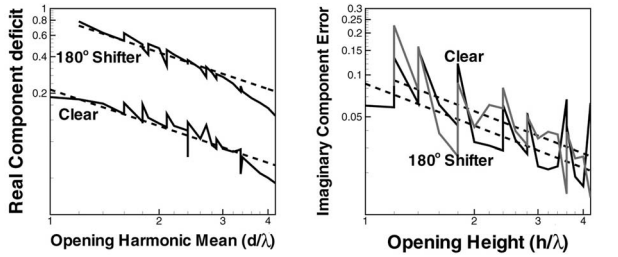

Fig. 5. (a) Log-log plot of the relative error in the real component of the electric field on the wafer produced by the thin-mask approximation, as compared with the rigorously evaluated EM field, versus the harmonic mean of the opening height and width. (b) Log-log plot of the relative error in the imaginary component as a function of opening height (opening size in the direction perpendicular to polarization).

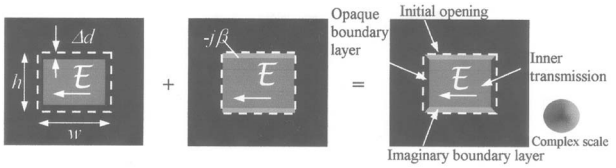

Fig. 6. (a) Real component of the BL model. (b) Imaginary component of the BL model. (c) Final BL model as the superposition of both real and imaginary parts.

Table 1. Width and Transmission Coefficients of the Boundary-Layer Model for Two Types of Reticle Cross Section in Typical Alternating-Phase-Shifting-Mask Geometry

Opening Type	Boundary Width (nm)	Tangential Boundary Transmission	Normal Boundary Transmission	Interior Transmission
Clear	24.8	0.8i	0	1
Shifter	53.0	−0.30i	0	−1

The corresponding parameters of width and transmission coefficient of the correction strip for the imaginary component of the field can also be deduced from the slope of the best fitting straight line to the data points, which is different for each type of etching profile. As indicated in Eq. (11), we chose to keep the correction strip width for the imaginary component equal to Δd in Eq. (10). This results in a final correction layer for the imaginary component of the field with a transmission coefficient equal to $-\beta$, on the aperture edges parallel to polarization. The correction to the total field is given by the superposition of the corresponding real and imaginary correction layers as illustrated in Fig. 6(c).

$$\text{Relative imaginary error} = \text{Im}\left\{\frac{\Delta \mathbf{E}}{\mathbf{E}}\right\} = -\beta\frac{2\Delta d}{h}, \tag{11}$$

Thus the final model, which we call the boundary-layer (BL) model, has a purely imaginary transmission coefficient that is proportional to the absolute value of the cosine angle between the electric field polarization and the edge direction, reaching its maximum value when the electric field is tangent to the boundary, and diminishing to zero when the field is normal to it. This simple geometric rule (cosine rule) accounts for the orientation dependence of the boundary conditions at the metal edges.

The key result of our simulations is that the thick-mask effects can be interpreted to a good approximation as an intrinsic edge property, as initially suggested by Young, and modeled with just two fixed parameters: width and transmission coefficient of a locally applied boundary layer. Usually, the width of the boundary layer controls the variation in peak amplitude, while the imaginary transmission coefficient corrects phase deviations of the thick mask. These errors differ for different types of mask edge cross sections, giving rise to different boundary-layer parameters to be applied locally in the vicinity of each type of mask edge profile. Hence each mask edge specification (clear or 180° shifter) has its own set of boundary layer parameters derived from the slope of the best fitting straight line to the error data points, and collected in Table 1. These errors also vary with the chrome thickness and index of refraction. Thus the model requires new sets of parameters to be calculated, through more rigorous 3D electromagnetic simulations, whenever the mask profile is modified.

4. BOUNDARY-LAYER APPROXIMATION

The conclusions of Section 3 provided the basis for the development of a simple BL model to account for electromagnetic effects in lithographic reticles. This model consists of a sophisticated version of the Kirchhoff or thin-mask approximation, simply adding a layer of fixed width and transmission at every edge. The BL parameters were optimized for the field component along the direction of polarization of the incident light E_x for both amplitude and phase. This is illustrated in Fig. 7(a), where the

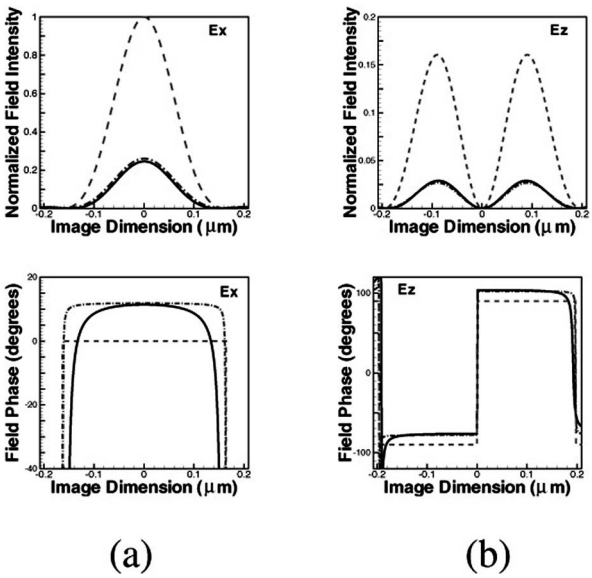

Fig. 7. Comparison between the aerial field components produced by rigorously evaluated EM TEMPEST field solutions of the object field (solid curves) and both the corresponding thin-mask approximation (dashed curves) and our BL model (dashed–dotted curves), of a 1.6λ, 180°-phase-shift square mask opening. (a) Intensity and phase of the field component along the polarization direction (x axis); (b) intensity and phase of the field coupled to the component along the optical axis (z axis).

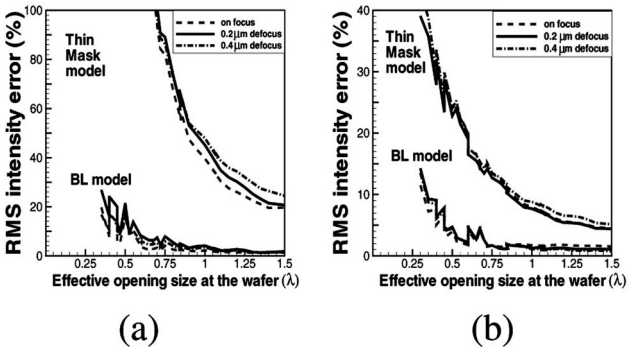

Fig. 8. Rms error in the intensity distribution, integrated over the focal plane and at two out-of-focus positions, of the approximated images relative to the rigorous EM fields for unpolarized, partially coherent illumination at 193 nm, NA=0.85, σ=0.6. (a) 180°-phase-shift openings; (b) clear openings.

aerial images of the rigorously evaluated mask fields (solid curves) are contrasted with their corresponding thin-mask (dashed curves) and BL (dashed–dotted curves) approximations of a 180°-phase-shifting, isolated, square aperture of side length 1.6λ illuminated with normal, coherent illumination at 193 nm and imaged by a 4× reduction system of NA=0.85. The same BL parameters, however, provided similar error reductions for all cross-field coupled components arising at the exit pupil of a high-NA lens.

Figure 7(b) illustrates an example of accurate fit of the BL approximation to the rigorous field coupled along the optical axis E_z. Moreover, the BL model provided error reductions relative to the Kirchhoff approximation of 5× to 10× in all field components, as measured by the rms error on the field intensity integrated over the wafer plane area, for both clear and 180°-shifter openings of dimensions ranging from 1λ to 6λ for both 193 nm and 248 nm lithography.[15]

Illumination in industrial applications consists of an unpolarized source of partially coherent light that reduces some of the effects associated with coherent illumination. Under the assumption of Köhler illumination configuration[1] and based on the discretization of the source into a number of spatially incoherent point sources, imaging with partially coherent illumination in lithography is modeled as the superposition of incoherent plane waves impinging on the reticle at different incident angles. Typical printing situations encountered in optical lithography involve reduction factors of 4× or 5× and partial coherence factors of σ between 0.3 and 0.8, and therefore incident angles no larger than 10° with respect to the normal direction. Under such circumstances the harmonics diffracted by the reticle remain approximately constant and equal to those obtained at normal incidence, except for the corresponding shift in frequency,[16] thus allowing the utilization of the same BL parameters deduced for normal incidence in Section 3 for the off-axis components.

Unpolarized (both TE and TM components were added incoherently), conventional, partially coherent illumination was used at 193 nm with a system of NA=0.85 and σ=0.6 to simulate the aerial images due to the range of isolated spaces with sizes between 1λ and 6λ on the mask analyzed in Section 3. The rms error in the intensity distribution integrated over the wafer plane area was calculated for the aerial images generated by the modeled mask fields relative to the rigorous electromagnetic fields. Figures 8(a) and 8(b) are plots of the rms error for the clear and 180°-shifter openings, respectively. Some of the points in the plots show slightly larger rms errors. They correspond to rectangular apertures with high aspect ratios, which also showed the largest deviations from the fitting inverse line of the imaginary error in Fig. 5(b). Provided that transmission loss through the aperture on the thick mask is the main source of error, the use of the BL model on these points provides similar error improvements relative to the thin-mask approximation for both square and rectangular openings. In order to evaluate the effect of phase deviations, rms errors are evaluated at the focal plane and at two out-of-focus planes in Fig. 8. No significant variation of the error is observed for defocus amounts up to 0.4 μm, proving the accuracy of the BL model within typical values of depth-of-focus.

Our BL model was also applied to dense periodic mask features such as those of Fig. 9. Figure 9(a) represents the Kirchhoff scalar approximation (thin-mask model) of a 78 nm (1×) half-pitch array of alternating 180°-shifter and clear lines. Figure 9(b) shows a sketch of the actual object field obtained by rigorous electromagnetic FDTD TEMPEST simulation on the mask plane of the same mask pattern and vertically polarized electric field. Finally, Fig. 9(c) shows the BL model for the same mask features and illumination conditions.

Figures 10(a)–10(c), on the other hand, correspond to the aerial image intensity at the focal plane for the rigorously evaluated object field of Fig. 9(b) and its two modeling approaches. Unpolarized, σ=0.5 partially coherent il-

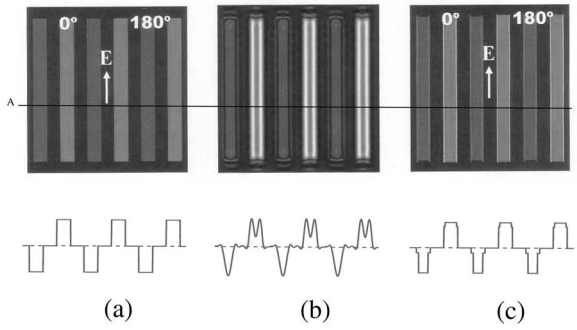

Fig. 9. (a) Kirchhoff scalar approximation (thin-mask model) of the field on the mask plane of a 78 nm (as measured at the wafer plane), half-pitch array of alternating 180°-shifter and clear line openings, with vertically polarized electric field at 193 nm. (b) Sketch of the actual object field obtained by rigorous electromagnetic FDTD TEMPEST simulation on the same mask. (c) BL model for the same mask features and illumination conditions. A cross-sectional view of the mask field for each case along cut A is displayed at the bottom for clarity.

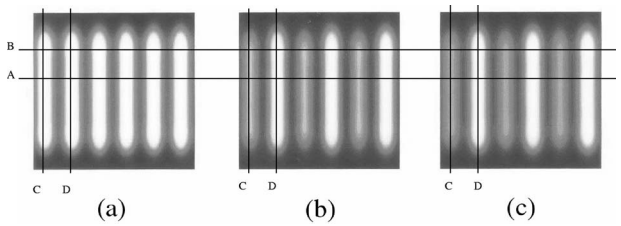

Fig. 10. Aerial image intensity results at the focal plane of a 78 nm (as measured at the wafer plane), half-pitch array of alternating 180°-shifter and clear mask lines with an unpolarized, $\sigma=0.5$, partially coherent illumination at 193 nm and NA=0.85. (a) Aerial image produced by the thin-mask approximation with an rms error of 50.97%. (b) Aerial image produced by the rigorously evaluated object field. (c) Aerial image produced by the BL model with an rms error of 4.63%.

lumination at 193 nm was used with a NA=0.85 imaging system. Figures 10(b), produced by the rigorously evaluated object field, and 10(c), corresponding to the BL model, show close agreement, with an rms error of only 4.63% due to the approximation. However, Fig. 10(a), obtained from the thin-mask approximation, produced a much higher rms error of 50.97% as compared with the actual image.

The cross-sectional planes marked in Fig. 10 by the lines A, B, C, and D are plotted in Figs. 11(a)–11(l). These views are plotted for the three aerial images at the focal plane (left) as well as at 0.2 μm (center) and 0.4 μm (right) defocus. All of the plots reveal a close overlap between the rigorous solutions and those obtained through the BL model, even at points close to the line ends. This improved modeling accuracy appears to be independent of the pitch value according to the plot in Fig. 12 of the rms error measured for different pitches at the wafer plane.

As a final example of our model performance on square corners, the mask pattern of Fig. 13 is analyzed. As before, Fig. 13(a) depicts the Kirchhoff scalar approximation of the field on the mask plane of a 79 nm (as measured at the wafer plane) half-pitch array of alternating 180°-shifter and clear lines that form a 90° corner. Figure 13(b) illustrates the actual object field with vertically polarized electric field at 193 nm, obtained by rigorous electromagnetic FDTD TEMPEST simulation on the same mask. Figure 13(c) represents the BL model for the same mask features and illumination conditions.

Aerial image intensity results at the focal plane for the mask pattern of Figs. 14(a)–14(c) were calculated for unpolarized light and an imaging system of $\sigma=0.4$, partially coherent illumination at 193 nm, and NA=0.85. The enhanced modeling accuracy due to the boundary layer can

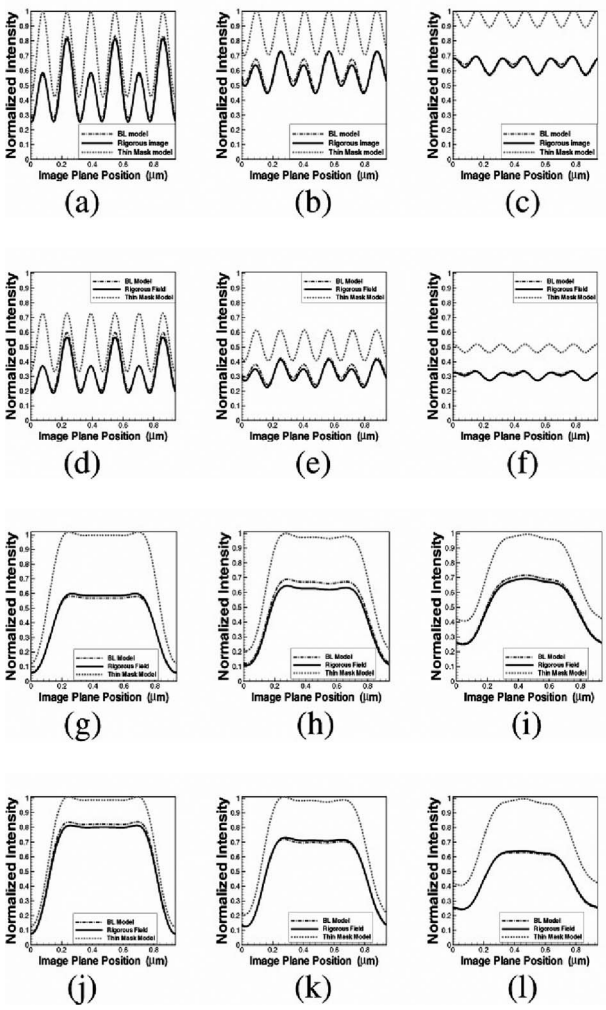

Fig. 11. Cross-sectional view along the cuts of Fig. 10: (a)–(c) cut A; (d)–(f) cut B, (g)–(i) cut C, (j)–(l) cut D. Figures on the left-hand side show the image at the focal plane; figures at the center and right-hand side display the effect of defocus at 0.2 μm out-of-focus and 0.4 μm out-of-focus, respectively.

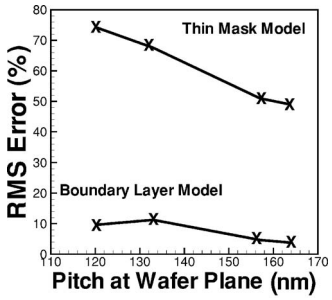

Fig. 12. Rms error integrated over the wafer plane of periodic lines with different pitch dimensions, modeled by either the thin-mask or the BL models.

Fig. 13. (a) Kirchhoff scalar approximation (thin-mask model) of the field on the mask plane of a 79 nm (as measured at the wafer plane), half-pitch array of alternating 180°-shifter and clear corner openings, with vertically polarized electric field at 193 nm. (b) Sketch of the actual object field obtained by rigorous electromagnetic FDTD TEMPEST simulation on the same mask. (c) BL model for the same mask features and illumination conditions.

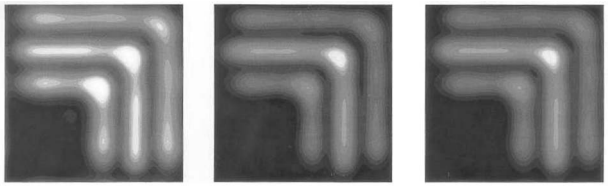

Fig. 14. Aerial image intensity results at the focal plane of a 79 nm (as measured at the wafer plane), half-pitch array of alternating 180°-shifter and clear square corners with an unpolarized, $\sigma=0.4$, partially coherent illumination at 193 nm and NA $=0.85$. (a) Aerial image produced by the thin-mask approximation with an rms error of 56.78%. (b) Aerial image produced by the rigorously evaluated object field. (c) Aerial image produced by the BL model with an rms error of 3.28%.

be appreciated directly from the plots. Quantitatively, the aerial image produced by the thin-mask approximation exhibits an rms error of 56.78%, while that produced by the BL model shows an error of 3.28%.

5. CONCLUSION

The physical theory of diffraction is a technique developed to correct for edge effects in the application of the physical-optics approximation on high-frequency scattering by perfectly conducting surfaces. It considers the effect of the edges as arising from some "fringe" line currents flowing along the object border. Lithographic reticles, however, cannot be regarded as perfect conductors given the finite index of refraction of the chrome layer at the operational wavelength, so a similar "fringe" edge-field concept was explored to account for the electromagnetic effects.

For rectangular apertures on both perfectly conducting plates and more realistic chrome layers of finite thickness and refractive index, we observed how the relative errors of the real and imaginary components of the field on the wafer follow an inverse law on the opening mean width and height, respectively. This allowed us to reduce the model to a simple boundary layer of fixed width and transmission coefficient. The proposed model, therefore, consists of a sophisticated version of the Kirchhoff approximation, simply adding a boundary layer to every edge, which greatly improves the accuracy of aerial image computation in photolithography simulations at a reasonable computational cost.

APPENDIX A: FRINGE FIELD ERROR IN OPTICAL LITHOGRAPHY

The fringe fields due to an aperture on a conducting plate can be expressed as[9]

$$\begin{aligned}\mathbf{E}^{\mathrm{FR}} &= -\eta\hat{\mathbf{r}}\times\mathbf{H}^{\mathrm{FR}}\\ &= -\eta\hat{\mathbf{r}}\times\int_{C'}2[(-\mathbf{H}^{\mathrm{inc}}\cdot\hat{\mathbf{l}}')\mathbf{F}(l',\hat{\mathbf{r}})\\ &\quad+\eta^{-1}(\mathbf{E}^{\mathrm{inc}}\cdot\hat{\mathbf{l}}')\mathbf{G}(l',\hat{\mathbf{r}})]\frac{e^{ikr}}{4\pi r}\mathrm{d}l',\end{aligned}\tag{A1}$$

where $r=|\hat{\mathbf{r}}-\hat{\mathbf{r}}'|$ and the term between brackets represents the edge wave emanating from each differential element of the edge. This edge wave is a function of the incident electric and magnetic fields multiplied by the direction vector coefficients $\mathbf{F}$ and $\mathbf{G}$,[12] which are trigonometric functions dependent on the incident point on the object boundary l' and the observation direction $\hat{\mathbf{r}}$. The unit vector $\hat{\mathbf{l}}'$ is tangent to the edge at every point. Assuming normal incidence, Eq. (A1) was applied to the aperture of Fig. 2. The result was then assumed to propagate through a $4\times$ optical projection system of $\mathrm{NA}_o=0.85/4\sim0.2$ at the entrance pupil, and the corresponding peak amplitude was measured at the center of the image plane as illustrated in Fig. 2. The propagation distance r to the entrance pupil, assumed well into the far field of the aperture, is much larger than the wavelength, while the aperture dimensions considered here are of the order of the wavelength. This allows us to approximate the observation direction by the glancing incident direction, which yields $F\approx-1/2$ and $G\approx1/2$ after the singularities cancel out in Ufimtsev's formulation. Therefore, with the change of variables of $f=r_x/\mathrm{NA}$ and $g=r_y/\mathrm{NA}$ and dropping the constant phase factors, the image fields at the focal plane will be given by

$$\begin{aligned}\mathbf{E}^{\mathrm{FR}}_{\mathrm{image}}(x,y) &= -\eta\hat{\mathbf{r}}\times\hat{\mathbf{x}}\Bigg\{H_o 2h\mathrm{NA}^2\int\int_{f^2+g^2\le1}\cos(\pi\mathrm{NA}gw)\\ &\quad\times\mathrm{sinc}(\pi\mathrm{NA}fh)e^{jk(fx+gy)}\mathrm{d}f\mathrm{d}g\frac{E_o}{\eta}2w\mathrm{NA}^2\\ &\quad\times\int\int_{f^2+g^2\le1}\cos(\pi\mathrm{NA}fh)\mathrm{sinc}(\pi\mathrm{NA}gw)e^{jk(fx+gy)}\mathrm{d}f\mathrm{d}g.\end{aligned}\tag{A2}$$

To first-order approximation, one can consider $\cos(\pi\mathrm{NA}gw)$, $\mathrm{sinc}(\pi\mathrm{NA}fh)$, $\cos(\pi\mathrm{NA}fh)$ and $\mathrm{sinc}(\pi\mathrm{NA}gw)\sim1$ within the integration limits of Eq. (A2), which is a reasonable approximation for small numerical apertures such as the one on the object side for imaging systems of high reduction factors. This approximation yielded the following expression of the fringe field at the image plane:

$$\mathbf{E}_{\text{image}}^{\text{FR}}(x,y) \simeq -\eta(\hat{\mathbf{r}} \times \hat{\mathbf{x}})H_o \frac{\text{NA}^2 J_1(k\sqrt{x^2+y^2})}{kr}(2h+2w), \tag{A3}$$

where $J_1(\alpha)$ represents the Bessel function of the first kind, order 1, such that, at the center of the image, $J_1(x)/x = 1/2$ with $x = 0$. As a final step, one can extract the main polarization component E_y from Eq. (A3) and assume $r_z \approx 1$ for 4× optical reduction, to obtain

$$E_{\text{image}}^{\text{FR}} \simeq -E_o \frac{\text{NA}^2 J_1(k\sqrt{x^2+y^2})}{kr}(2h+2w). \tag{A4}$$

A similar analysis was carried out on the Kirchhoff component of the total field to derive the main polarization component of the image field expression on the focal plane, which resulted in

$$E_{\text{image}}^{\text{K}} \approx -jk2E_o hw \frac{\text{NA}^2 J_1(k\sqrt{x^2+y^2})}{kr}. \tag{A5}$$

The final relative error due to the fringe fields at the image focal plane is calculated as $\Delta E/E = E_{\text{image}}^{\text{FR}}/E_{\text{image}}^{\text{K}}$.

ACKNOWLEDGMENTS

The authors are very grateful to Xuelong Shi of MaskTools for providing some important references. This work was supported by grant DAAD19-99-1-0196 from U.S. Department of the Army and by the La Caixa Foundation Scholarship Program (Spain).

Corresponding author J. Tirapu-Azpiroz's e-mail address is jaionet@us.ibm.com.

REFERENCES

1. M. Born and E. Wolf, *Principles of Optics* (Pergamon, 1987).
2. H. J. Levinson, *Principles of Lithography* (SPIE, 2001).
3. M. D. Levenson, N. S. Viswanathan, and R. A. Simpson, "Improving resolution in photolithography with phase shifting-mask," IEEE Trans. Electron Devices **ED-29**, 1828–1836 (1982).
4. C. Pierrat and A. Wong, "The MEF revisited: Low k1 effects versus mask topography effects," in *Optical Microlithography XVI*, A. Yen, ed., Proc. SPIE **5040**, 193–202 (2003).
5. M. S. Yeung and E. Barouch, "Limitation of the Kirchhoff boundary conditions for aerial image simulation in 157 nm optical lithography," IEEE Electron Device Lett. **21**, 433–435 (2000).
6. P. Y. Ufimtsev, Method of Edge Waves in the Physical Theory of Diffraction (Foreign Technology Division, Air Force Systems Command, 1971).
7. K. Adam and A. R. Neureuther, "Simplified models for edge transitions in rigorous mask modeling," in *Optical Microlithography XIV*, C. J. Progler, ed., Proc. SPIE **4346**, 331–344 (2001).
8. A. Khoh, G. S. Samudra, W. Yihong, T. Milster, and B.-I. Choi, "Image formation by use of the geometrical theory of diffraction," J. Opt. Soc. Am. A **21**, 959–967 (2004).
9. J. Tirapu-Azpiroz, "Analysis and modeling of photomask near-fields in subwavelength deep ultraviolet lithography," Ph.D. dissertation (University of California at Los Angeles, 2004).
10. C. T. Tai, "Direct integration of field equations," Electromagn. Waves: Prog. Electromagn. Res. **28**, 339–359 (2000).
11. P. Y. Ufimtsev, "Rubinowicz and the modern theory of diffracted rays," Electromagnetics **15**, 547–565 (1995).
12. P. Y. Ufimtsev, "Elementary edge waves and the physical theory of diffraction," Electromagnetics **11**, 125–160 (1991).
13. J. Tirapu-Azpiroz and E. Yablonovitch, "Modeling of near-field effects in sub-wavelength deep ultraviolet lithography," in *Future Trends of Microelectronics 2003*, S. Luryi, J. Xu, and A. Zaslavsky, eds. (Wiley-IEEE, 2004), pp. 80–92.
14. A. K. Wong and A. R. Neureuther, "Mask topography effects in projection printing of phase-shifting masks," IEEE Trans. Electron Devices **41**, 895–902 (1994).
15. J. Tirapu-Azpiroz and E. Yablonovitch, "Fast evaluation of photomask near-fields in sub-wavelength 193 nm lithography," Proc. SPIE **5377**, 1528–1535 (2004).
16. T. V. Pistor, A. R. Neureuther, and R. J. Socha, "Modeling oblique incidence effects in photomasks," in *Optical Microlithography XIV*, C. J. Progler, ed., Proc. SPIE **4000**, 228–237 (2000).